JACS
JOURNAL OF THE AMERICAN CHEMICAL SOCIETY

ARTICLE

pubs.acs.org/JACS

Interplay of Three-Dimensional Morphologies and Photocarrier Dynamics of Polymer/TiO_2 Bulk Heterojunction Solar Cells

Shao-Sian Li,[†,⊥] Ching-Pin Chang,[†,‡,⊥] Chih-Cheng Lin,[†] Yun-Yue Lin,[†] Chia-Hao Chang,[†] Jer-Ren Yang,[†] Ming-Wen Chu,[‡] and Chun-Wei Chen*[,†]

[†]Department of Materials Science and Engineering and [‡]Center for Condensed Matter Sciences, National Taiwan University, Taipei, 106, Taiwan

Supporting Information Web-Enhanced

ABSTRACT: In this study, we investigated the interplay of three-dimensional morphologies and the photocarrier dynamics of polymer/inorganic nanocrystal hybrid photoactive layers consisting of TiO_2 nanoparticles and nanorods. Electron tomography based on scanning transmission electron microscopy using high-angle annular dark-field imaging was performed to analyze the morphological organization of TiO_2 nanocrystals in poly(3-hexylthiophene) (P3HT) in optimal solar cell devices. The Three-dimensional (3D) morphologies of these hybrid films were correlated with the photocarrier dynamics of charge separation, transport, and recombination, which were comprehensively probed by various transient techniques. Visualization of these 3D bulk heterojunction morphologies clearly reveals that elongated and anisotropic TiO_2 nanorods in P3HT not only can significantly reduce the probability of the interparticle hopping transport of electrons by providing better connectivity with respect to the TiO_2 nanoparticles, but also tend to form a large-scale donor−acceptor phase-separated morphology, which was found to enhance hole transport. The results support the establishment of a favorable morphology for polymer/inorganic hybrid solar cells due to the presence of the dimensionality of TiO_2 nanocrystals as a result of more effective mobile carrier generation and more efficient and balanced transport of carriers.

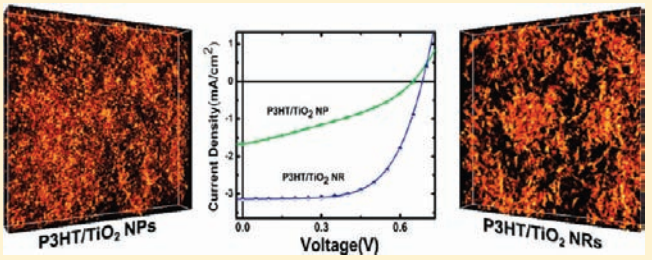

In the past decade, polymer solar cells have attracted great interest in the development of low-cost, large-area, and mechanically flexible photovoltaic devices.[1−3] Due to the short exciton diffusion length (∼10 nm) of a semiconducting polymer,[4] the electron acceptors are usually intermixed with polymers (electron donors) at a nanometer length scale to form bulk heterojunctions (BHJs). Extensive research has focused on the development of polymer photovoltaic devices using fullerene or fullerene derivatives as acceptors, and recent advances have achieved high photovoltaic efficiencies in excess of 7%.[5] An alternative type of acceptor in polymer solar cells is based on inorganic semiconductor nanocrystals, taking advantage of their relatively high electron mobility and good physical and chemical stability. Various inorganic nanocrystals such as CdSe,[3,6] TiO_2,[7] PbS,[8] and ZnO[9] have been used in polymer/inorganic hybrid BHJ solar cells. In the class of inorganic acceptors, metal oxide nanocrystals such as TiO_2 and ZnO are two of the most promising materials since they are environmentally friendly and low-cost. Polymer solar cells based on various nanoscale morphologies of nanocrystal metal oxides, ranging from well-dispersed nanoparticles or nanorods[7,9] to well-connected nanoporous or aligned nanorod structures grown directly on substrates,[10−12] have been reported. Until now, the best polymer/metal oxide hybrid solar cells have been based on the BHJ architecture, blending dispersed nanocrystals within polymers. However, due to the strong incompatibility between inorganic nanocrystals and polymers, the precarious control of the BHJ morphology of the two intermixed components becomes more challenging than with the conventional polymer/fullerene hybrid solar cells. To overcome this drawback, Janssen et al. used the method of *in situ* generation of the inorganic semiconductor inside the organic material to control the morphology of poly(3-hexylthiophene) (P3HT)/ZnO nanoparticle hybrids, giving a best power conversion efficiency of 2.0%.[9] By contrast, we have recently demonstrated a power conversion efficiency of 2.2% for polymer solar cells based on P3HT/TiO_2 nanorod BHJs through an interface modification between P3HT and TiO_2 nanorods, and these hybrid films were deposited from the solution in a single step, similar to the common deposition methods.[7] In addition to the improvement of organic/inorganic interfaces, the nanocrystal shape is another parameter affecting the performance of polymer/inorganic hybrid solar cells.[13,14] The morphological organization of differently shaped nanocrystals within a polymer matrix strongly affects the photocarrier dynamics of the active layers and thus the photovoltaic performance. Recently, three-dimensional (3D) electron tomography has become an ideal tool for gaining insight into the nanoscale organization of BHJ polymer solar cells, providing the critical morphological parameters for improving the device performance.[9,13,15,16] Here,

Received: April 6, 2011
Published: June 18, 2011

dx.doi.org/10.1021/ja203151z | *J. Am. Chem. Soc.* 2011, 133, 11614–11620

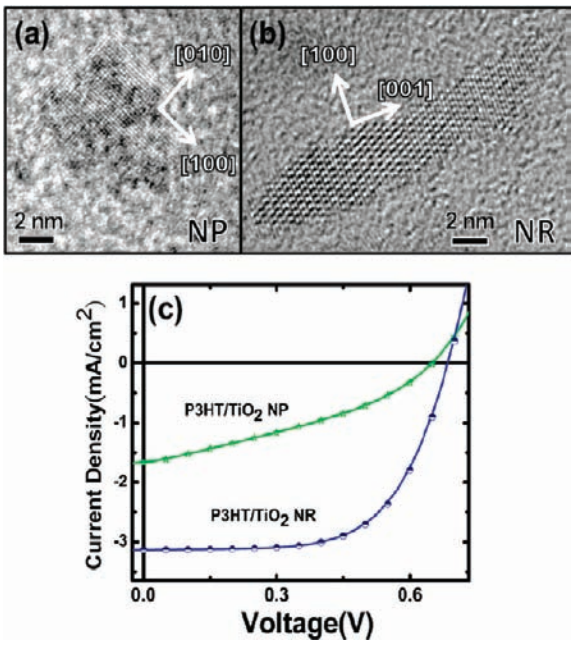

Figure 1. High-resolution TEM image of TiO_2 (a) NPs and (b)NRs. (c) Current−voltage characteristics of P3HT/TiO_2 NP (green) and NR (blue) hybrid solar cell devices.

we employed electron tomography based on scanning transmission electron microscopy using high-angle annular dark-field (STEM-HAADF) imaging to probe the 3D morphological organization of P3HT/TiO_2 hybrid BHJs with different nanocrystal shapes, including nanoparticles (NPs) and nanorods (NRs). We also performed a comprehensive analysis of the photocarrier dynamics corresponding to the 3D structures of these blends, including charge separation, transport, and recombination as probed by various transient techniques including time-resolved photoluminescence (TRPL) spectroscopy, transient open-circuit voltage decay (TOCVD) measurements, time-of-flight (TOF) techniques, and photo-assisted charge extraction with a linearly increasing voltage (photo-CELIV) measurements. The interplay between the nanocrystal shape-dependent 3D morphology and the photocarrier dynamics enables us to understand the key factors to further improve the device performance of polymer/inorganic hybrid solar cells.

The growth of the anatase TiO_2 NPs and NRs that were synthesized is described in the Supporting Information (SI). Figure 1a,b shows high-resolution transmission electron microscopy (HRTEM) images of the TiO_2 nanocrystals with a characteristic size of ∼5 nm for the NPs and ∼4 nm (diameter) × ∼20 nm (length) for the NRs, respectively. The as-synthesized TiO_2 NPs and NRs are usually capped with an insulating surfactant of oleic acid (OA), consisting of a long alkyl chain, which acts as a potential barrier for the charge transfer. In this study, we used ligand exchange treatment by pyridine on both TiO_2 NPs and NRs to remove the original OA surfactant to improve the device performances.[7] We fabricated the photovoltaic devices by spin-coating the photoactive layers, which consisted of P3HT/TiO_2 NP and NR hybrids on top of the ITO/PEDOT:PSS anode electrode. The Al electrode was then deposited onto the active layer by thermal evaporation. Various weight ratios of P3HT to TiO_2 nanocrystals were tested under similar conditions, and the optimal device performance for both P3HT/TiO_2 NP and NR hybrid thin films could be obtained with a 50:50 (wt %) ratio. The morphology of the P3HT/TiO_2 hybrid thin films became poor when the concentration of TiO_2 NPs or NRs was larger than 70 wt %, when a large aggregation of nanocrystals can be observed using the optical microscope. Figure 1c shows the current−voltage characteristics of photovoltaic devices under a simulated A.M. 1.5 illumination (100 mW/cm^2). The device based on the P3HT/TiO_2 NP hybrid thin film exhibits a short-circuit current density (J_{sc}) of 1.65 mA/cm^2, an open-circuit voltage (V_{oc}) of 0.60 V, and a fill factor (FF) of 0.42, resulting in a power conversion efficiency (η) of 0.42 %. By contrast, the P3HT/TiO_2 NR hybrid device shows a largely improved photovoltaic performance, with J_{sc} = 3.10 mA/cm^2, V_{oc} = 0.69 V, and FF = 0.62, giving η = 1.33%. The better-performing P3HT/TiO_2 NR hybrid device compared to its NP counterpart indicates that nanocrystal shape can largely affect device performance. In particular, the relatively high FF = 0.62 of the P3HT/TiO_2 NR hybrid device suggests that a favorable BHJ morphology may exist for efficient carrier transport or collection. Understanding how the organization of these differently shaped nanocrystals within the polymer affects the corresponding photocarrier dynamics and the photovoltaic performance of the P3HT/TiO_2 hybrid solar cells is of great interest.

Next, we performed STEM-HAADF electron tomography to reveal the 3D morphologies of TiO_2 NPs and NRs in P3HT. For a BHJ solar cell, the formation of a nanoscale bicontinuous donor−acceptor network is crucial to obtain efficient photovoltaic performance.[17] Therefore, determining the exact 3D features of the embedded donor and acceptor materials is of vital importance. Electron tomography, with its unparalleled nanometer-scale resolution in 3D imaging, is an indispensable technique for unraveling this problem. Visualization of the 3D transport pathways for holes or electrons has been recently demonstrated in various types of hybrid solar cells using TEM tomography.[9,16] However, the focus-dependent phase/diffraction contrasts inherent to TEM imaging are susceptible to artifact creations in the associated 3D reconstructed volumes.[15,18,19] Regarding this aspect, STEM-HAADF imaging represents an optimal solution because the corresponding contrast is purely incoherent and arises from thermal diffused scattering, which is ultimately amplitude contrast (sensitive to atomic numbers only) and is robust to electro-optical focusing conditions, unlike TEM.[13,18−20] The interpretation of images in STEM-HAADF is thus straightforward, with the dark (bright) contrasts attributed to light (heavy) matter, that is, P3HT for the dark contrasts and TiO_2 for the bright ones in our current case. Figure 2a,b shows snapshots of the 3D reconstructed grayscale images of P3HT/TiO_2 NP and NR hybrid thin films, respectively. The two reconstructed images show very different nanoscale morphologies of TiO_2 nanocrystals distributed in P3HT. The intermixing between TiO_2 NPs and P3HT is found to be more significant than in the P3HT/TiO_2 NR hybrid. By contrast, a larger scale of phase separation, consisting of several more distinct TiO_2 NR-rich clusters separated by P3HT domains, can be clearly observed in the P3HT/TiO_2 NR hybrid thin film. Figures 2c,d further exhibits these tomography images viewed from different angles. Because the photogenerated carriers are expected to be transported through the films and collected at the top and bottom electrodes, the morphological organization of TiO_2 nanocrystals along the direction perpendicular to the substrate is the most important when determining the photovoltaic performance. We have further sliced the reconstructed volumes to gain insight into

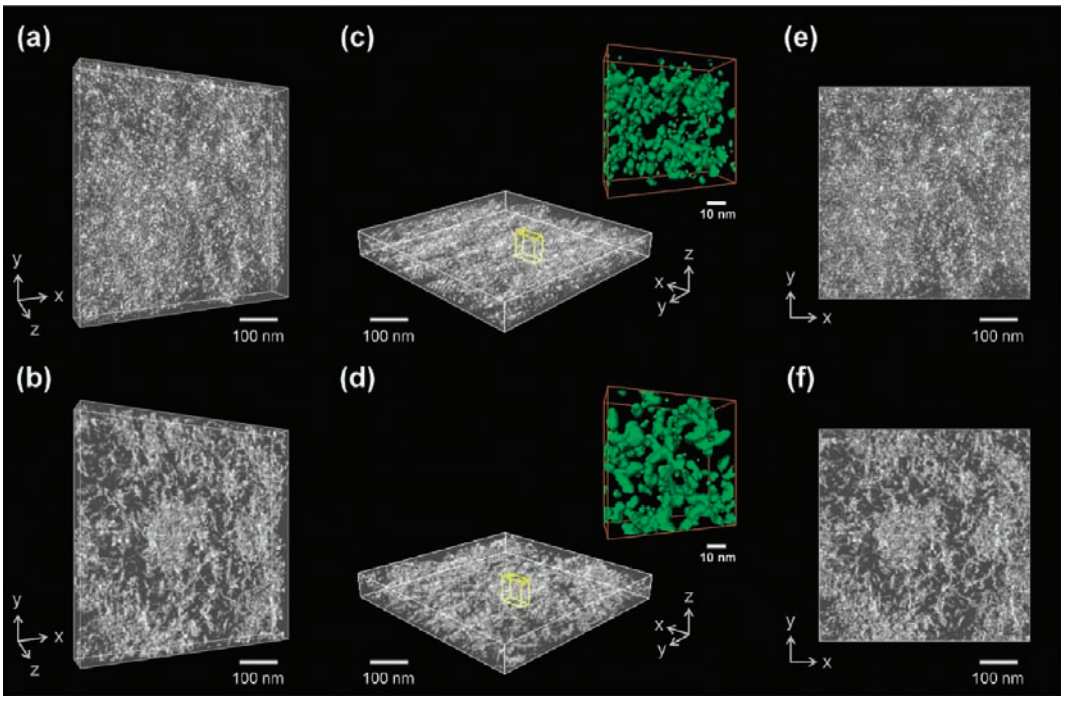

Figure 2. W STEM-HAADF electron tomography images of the P3HT/TiO_2 NP (a,c) and NR (b,d) hybrid thin films viewed from different angles. The dimension of these films is about 570 nm × 570 nm × 70 nm. The insets in (c) and (d) show the connective networks along the film direction formed by TiO_2 NPs and NRs. The size of these two slices is about 70 nm × 30 nm × 70 nm. (e,f) 2D projection images of the respective 3D view-graphs in (a) and (b) along the film thickness direction. Video files of all the reconstructed volumes and slices lying in the horizontal planes of the NP (movie 1) and NR (movie 2) hybrid films are available in the online (HTML) version of this article.

the information of the connective networks along the vertical direction formed by TiO_2 NPs and NRs, as shown in the insets of Figure 2c,d, conducted by the surface rendering method with the contrast threshold set to remove the low-background contrast resulting from the P3HT matrix. It is clearly seen that the anisotropic TiO_2 NRs can largely reduce the number of junctions of a connective network compared to the TiO_2 NPs, which are isotropic without any preferred orientation. The aspect ratio of the TiO_2 NRs with preferred orientations angled toward the plane of the film provides a better chance for them to form a connective network between two electrodes. This has the advantage of reducing the probability of interparticle hopping and facilitating carrier transport. Figure 2e,f further exhibits two-dimensional projection images of the respective 3D view-graphs along the film thickness direction, where a larger amount of phase-separated TiO_2 NR-rich domains surrounded by P3HT can be clearly observed. The corresponding video files of all the rotating 3D reconstructed volumes and slices lying in the horizontal planes of the P3HT/TiO_2 NP and NR hybrid films are available in the online (HTML) version of this article. It is noted that the optimal morphology of the P3HT/TiO_2 NR hybrid solar cell is very different from that of another widely studied polymer/inorganic hybrid solar cell using CdSe NRs, where a much higher concentration of CdSe NRs was used due to their contribution to light harvesting.[13,14] In addition, it is also found that the dispersion of TiO_2 nanocrystals in our system is less homogeneous as compared to the optimal morphology in the P3HT/ZnO NP hybrid solar cells using the method based on *in situ* generation of the inorganic nanocrystals inside the organic material to reduce aggregation.[9] Therefore, the above tomography analyses clearly reveal two pieces of important 3D morphological information about P3HT/TiO_2 BHJs: (i) the presence of dimensionality of the TiO_2 nanocrystals in P3HT enables the formation of an interconnecting network that can provide better connectivity due to the anisotropy, and (ii) the P3HT/TiO_2 NR hybrid is favored to form large-scale donor−acceptor separated phases compared to its NP counterpart. The significantly improved performance of the P3HT/TiO_2 NR hybrid device over its NP hybrid counterpart may be qualitatively attributed to the establishment of a favorable 3D morphology that more closely resembles the ideal bicontinuous donor−acceptor phase-separated morphology of typical high-performance polymer solar cells.

To further quantitatively correlate the nanocrystal-shape dependent morphology to the photovoltaic performance, we carried out a series of transient measurements to investigate the photocarrier dynamics of these P3HT/TiO_2 nanocrystal BHJ hybrid films. The performance of polymer photovoltaic devices is known to be largely influenced by the mechanisms of charge separation, transport, and recombination, which are strongly dependent on the film morphology. The charge separation of a polymer is usually a two-step process where excitons are first separated to less strongly bound electron−hole pairs and finally to free carriers.[21] We performed TRPL spectroscopy to examine the exciton dissociation efficiency in the P3HT/TiO_2 NP and NR hybrid thin films, as shown in Figure 3a. The addition of TiO_2 nanocrystals in polymer usually resulted in a new relaxation process, which provided the donor (P3HT) with a further nonradiative process and led to quenching of PL emission and shortening of the measured lifetime τ_{PL}. The PL was largely quenched after TiO_2 nanocrystals were added to P3HT (inset), which was accompanied with a much shorter PL decay time. The decay time for the pristine P3HT is 650 ps. The P3HT/TiO_2 NP

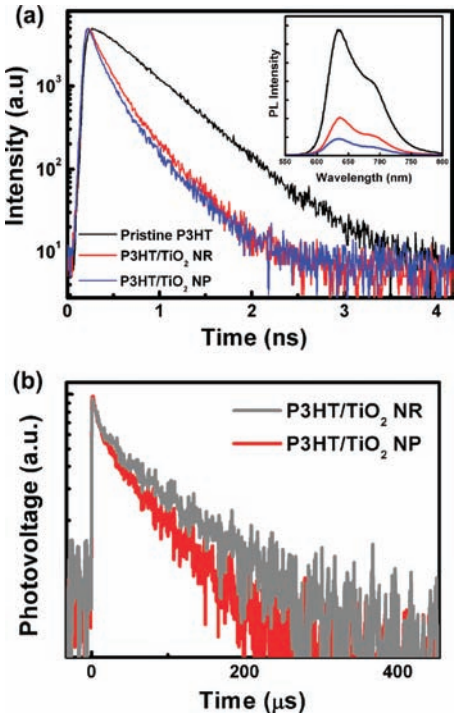

Figure 3. (a) TRPL spectroscopy of pristine P3HT and P3HT/TiO_2 NR and NP hybrids. The inset shows the PL intensities of these samples. (b)Transient photovoltage decay curves of the P3HT/TiO_2 NR and NP hybrid solar cell devices in the TOCVD measurement.

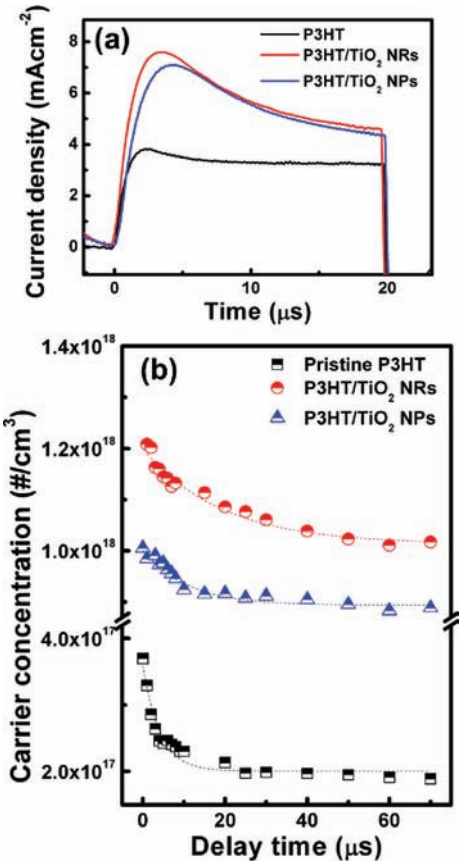

Figure 4. (a) Typical photo-CELIV transient curves derived from P3HT and P3HT/TiO_2 NR and NP hybrid devices. (b) Carrier concentrations of these devices derived from different delay times with exponentially fitting curves.

hybrid had a lower yield of PL emission (inset) and a shorter PL decay lifetime of 232 ps, compared to 251 ps in the P3HT/TiO_2 NR hybrid, indicating more efficient exciton dissociation. The morphology data showed that a large number of interfaces between P3HT and TiO_2 NPs existed due to the higher intermixing compared to that in the P3HT/TiO_2 NR hybrid. The average distance of an exciton generated in a polymer diffusing to the heterojunctions is expected to be shorter as a result of more efficient exciton dissociation in the P3HT/TiO_2 NP hybrid than in the NR counterpart. After exciton dissociation, electrons and holes either recombined at the P3HT/TiO_2 interfaces or became free carriers to be transported through the conducting paths formed by the TiO_2 nanocrystals and P3HT, respectively. Next, we performed the TOCVD measurement to determine the recombination rate at the interfaces of the P3HT and TiO_2 nanocrystals using the operating photovoltaic devices. In the TOCVD measurement, the devices operated at the open-circuit condition (V_{oc}) under the white light bias source. Since no charge was collected at the V_{oc} condition, a small perturbation generated by a pulsed laser was used to generate extra electrons and holes in hybrids. The extra electrons and holes recombined at the P3HT/TiO_2 nanocrystals interfaces with a lifetime τ_{rec}, resulting in the decay of the transient photovoltage. Figure 3b shows the photovoltage decay curves of the devices based on the P3HT/TiO_2 NR and NP hybrids. The P3HT/TiO_2 NR hybrid device shows a slower recombination rate at the interfaces with a longer τ_{rec} = 77.4 μs, compared to the P3HT/TiO_2 NP hybrid device with τ_{rec} = 54.3 μs. In a previous study, we showed that the interfacial ligand molecules on the TiO_2 nanocrystal surface can significantly affect the recombination rates at the P3HT/TiO_2 interfaces.[7] Although the same interface modification treatment was performed in both TiO_2 NPs and NRs in this study, the lower recombination rate for the P3HT/TiO_2 NR hybrid device can be mainly attributed to (i) the overall smaller interface area between the P3HT and TiO_2 NRs compared to the P3HT/TiO_2 NP hybrid, which may reduce the recombination probability in the surface states or traps,[22] or (ii) more effective distancing of the electrons and holes from the dissociation sites after charge separation, even in the absence of an internal electric field, as a result of the establishment of a more favorable morphology of the optimal P3HT/TiO_2 NR hybrid device.

Once these photogenerated carriers are separated as free electrons and holes, they either have to be transported to their respective electrodes by the built-in electric field of the device or undergo recombination. The holes are expected to be transported through the P3HT chains and the electrons along the TiO_2 nanocrystals. We therefore carried out the photo-CELIV measurement and TOF measurement to determine the carrier concentration, recombination lifetime, and mobility of the hybrid films. The photo-CELIV technique simultaneously enables the determination of the mobility and recombination rate of free carriers in real photovoltaic devices. It employs a pulsed laser to excite photogenerated carriers inside the active material, followed by an extraction of the free carriers using a triangular voltage ramp with a reverse bias and a controlled delay time.[23−25] The typical transient curves of the pristine P3HT, P3HT/TiO_2 NR, and P3HT/TiO_2 NP devices are shown in Figure 4a. The

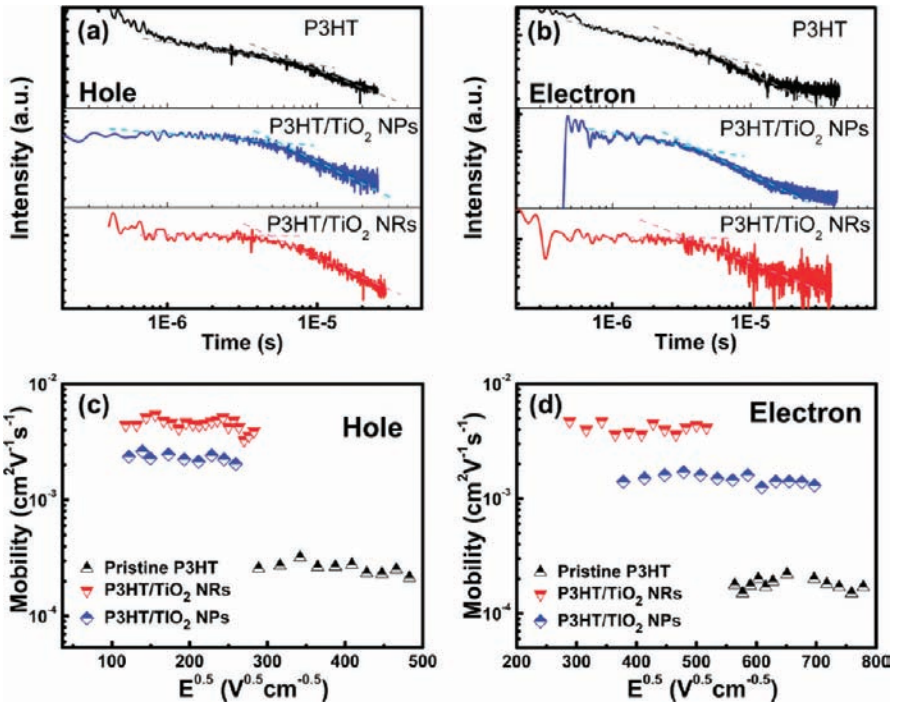

Figure 5. Typical double-logarithmic plots of TOF transient photocurrent for (a) hole and (b) electron transport. The transit time t_{tr} can be estimated from the intersection point in the double-logarithmic plot. Field-dependent mobilities of (c) hole and (d) electron of P3HT and P3HT/TiO_2 NR and NP hybrid films.

variations in charge carrier concentrations of these devices are derived from the different delay times that can be estimated by integrating the conduction current over the extraction time according to eq (1) in the SI.[25] The P3HT/TiO_2 NR BHJ device exhibits higher carrier concentrations than the NP counterpart at all delay times. Although the initial photogenerated exciton dissociation in the P3HT/TiO_2 NP hybrid is more efficient, the establishment of a favorable morphology in the P3HT/TiO_2 NR hybrid enables the overall generation of mobile carriers to be transported toward electrodes more effectively, giving a higher carrier concentration. By fitting the concentration decay curve in Figure 4b, we are able to estimate the carrier recombination lifetime τ_R. The P3HT/TiO_2 NR hybrid device exhibits a longer τ_R = 23.5 μs, compared to the P3HT/TiO_2 NP counterpart with τ_R = 10.9 μs, indicating that a more efficient carrier transport and collection occurred. A very short τ_R = 4.13 μs was also observed in the pristine P3HT device, indicating that electrons and holes significantly recombined during the transport due to the lack of well-separated hole and electron transport paths. The prolonged recombination lifetime in the P3HT/TiO_2 NR hybrid device is also reflected in the enhanced carrier mobility as estimated from the transient curves according to eq (2) in the SI.[23,24] Because electrons and holes cannot be individually extracted by photo-CELIV measurement, the calculated mobility is mainly attributed to the contribution of two types of carriers. An effective mobility of about 9.1 $\times$ 10^{-4} $cm^2/V\cdot s$ (delay time =10 μs) was obtained from the P3HT/TiO_2 NR hybrid device, which is nearly 3 times that of the NP counterpart ($\sim$3.1 $\times$ 10^{-4} $cm^2/V\cdot s$, delay time =10 μs).

To further differentiate the effect of the 3D morphology on the efficiency of electron and hole transport, we performed the TOF technique, which is well-established for measuring charge mobility in organic thin films, to extract the unipolar carrier mobility of the electrons or holes. Figure 5a,b shows the typical hole and electron transient curves of pristine P3HT and P3HT/TiO_2 NR and NP hybrid thin films, respectively. The hole and electron transient photocurrent for the pristine P3HT is highly dispersive, and the typical transit time t_{tr} of the carriers can be estimated from the intersection point in the double-logarithmic plot. In contrast, the corresponding hole and electron transient photocurrent for the P3HT/TiO_2 NR and NP hybrids is less dispersive, with a more clearly defined plateau region. Figure 5c,d shows hole and electron mobilities μ of these thin films at different applied electric fields by plotting log μ versus the square root of the electric field ($\sqrt{E}$) in the Poole–Frenkel form.[26] All the samples show a very weak field dependence on the mobilities of electrons and holes. For the pristine P3HT sample, ambipolar transport with electron and hole mobilities in the range of (1–2) $\times$ $10^{-4}$$cm^2/V\cdot s$ were obtained, similar to the results reported in the literature.[27] The significantly increased electron mobility after addition of TiO_2 NRs or NPs to P3HT is mainly due to the formation of electron conductive pathways by TiO_2 nanocrystals. The electron mobility of the P3HT/TiO_2 NR hybrid is about 4.5 $\times$ 10^{-3} $cm^2/V\cdot s$ higher than the 1.2 $\times$ 10^{-3} $cm^2/V\cdot s$ of the P3HT/TiO_2 NP hybrid due to the formation of more effective conducting networks with a reduced number of interparticle hopping and a less dispersive electron transport. Most interestingly, the addition of TiO_2 NPs or NRs to P3HT also causes a large enhancement in hole mobility of the hybrid films, with less dispersive transport in comparison to the pristine P3HT. Since TiO_2 nanocrystals usually demonstrate very effective hole-blocking, the transport of holes in TiO_2 NRs or NPs in the hybrid films is unlikely.[28,29] In addition, it was demonstrated that the hole mobility of P3HT was enhanced by infiltration into the insulating nanopores,[30] which enables holes to be transported within the confined P3HT nanodomains.

Table 1. Summary of All the Photocarrier Dynamics Measured in This study by TRPL Spectroscopy, TOCVD Measurement, Photo-CELIV Measurement, and TOF Technique

	P3HT	P3HT/TiO_2 NP	P3HT/TiO_2 NR
exciton lifetime by TRPL (ps)	650	232	251
recombination lifetime by TOCVD (μs)	–	54.3	77.4
carrier transport lifetime by photo-CELIV (μs)	4.13	10.9	23.5
carrier mobility by TOF ($cm^2\ V^{-1}\ s^{-1}$)[a]			
hole	2.5×10^{-4}	2.2×10^{-3}	4.6×10^{-3}
electron	2.0×10^{-4}	1.2×10^{-3}	4.5×10^{-3}

[a] The TOF hole (electron) mobilities for P3HT and P3HT/TiO_2 NP and NR hybrid films were measured at electric fields of 1.6×10^5 (3.6×10^5), 4.0×10^4 (2.0×10^5), and 4.0×10^4 (2.0×10^5) V/cm, respectively.

Therefore, the change of P3HT morphology after addition of TiO_2 nanocrystals may be responsible for the increased hole mobility of the hybrid films. As observed from the above tomography images, the establishment of separate P3HT and TiO_2 nanocrystal transport pathways allows holes to move through the P3HT domains surrounded by the TiO_2 nanocrystals to reduce recombination and facilitate transport. Therefore, the P3HT/TiO_2 NR hybrid film that consists of more distinct donor−acceptor phases along the direction perpendicular to the substrate exhibits a higher hole mobility, around $4.6 \times 10^{-3} cm^2/V \cdot s$, than the P3HT/$TiO_2$ NP hybrid, with a mobility of 2.2×10^{-3} $cm^2/V \cdot s$. Although it should be noted that there might be some deviation of the absolute mobility values of the thin photovoltaic devices compared with the thicker TOF samples, the establishment of an optimal morphology comprising an elongated and anisotropic TiO_2 NR within the P3HT enables more efficient and balanced transport of both electrons and holes, which may account for the higher values of FF, J_{sc}, and η. Table 1 summarizes all the photocarrier dynamics results obtained in this study.

This work demonstrated the interplay between the 3D morphological organization of P3HT/TiO_2 nanocrystal hybrid solar cells and the corresponding photocarrier dynamics and photovoltaic performance. The presence of dimensionality of nanocrystals and the more distinct donor−acceptor separated phases in the P3HT/TiO_2 NR hybrids represents a favorable morphology for high-performance polymer solar cells, having more effective carrier generation, transport, and collection. Further improvements in device performance can be achieved by optimizing the sizes and shapes of the TiO_2 nanocrystals or aligning them to enhance carrier transport.

■ ASSOCIATED CONTENT

Supporting Information. Description of the synthesis of materials, device fabrication, and materials characterization. This material is available free of charge via the Internet at http://pubs.acs.org.

Web Enhanced Feature. Video files containing of all the rotating 3D reconstructed volumes and slices lying in the horizontal planes of the hybrid films are included in the online (HTML) version of this article.

■ AUTHOR INFORMATION

Corresponding Author
chunwei@ntu.edu.tw

Author Contributions
⊥These authors contributed equally to this work.

■ ACKNOWLEDGMENT

This work is supported by National Science Council, Taiwan (Project No. NSC 99-2119-M-002-012- and 96-2112-M-002-030-MY3). The authors thank Mr. Yun-Chieh Yeh for preparing TiO_2 NPs and NRs.

■ REFERENCES

(1) Ma, W.; Yang, C.; Gong, X.; Lee, K.; Heeger, A. J. *Adv. Funct. Mater.* **2005**, *15*, 1617–1622.
(2) Huynh, W. U.; Dittmer, J. J.; Alivisatos, A. P. *Science* **2002**, *295*, 2425–2427.
(3) Li, G.; Shrotriya, V.; Huang, J.; Yao, Y.; Moriarty, T.; Emery, K.; Yang, Y. *Nat. Mater.* **2005**, *4*, 864–868.
(4) Shaw, P. E.; Ruseckas., A.; Samuel, I. D. W. *Adv. Mater.* **2008**, *20*, 3516–3520.
(5) Liang, Y.; Xu, Z.; Xia, J.; Tsai, S. T.; Wu, Y.; Li, G.; Ray, C.; Yu, L. *Adv. Mater.* **2010**, *22*, E135–E138.
(6) Sun, B.; Snaith, H. J.; Dhoot, A. S.; Westenhoff, S.; Greenham, N. C. *J. Appl. Phys.* **2005**, *97*, 014914–6.
(7) Lin, Y. Y.; Chu, T. H.; Li, S. S.; Chuang, C. H.; Chang, C. H.; Su, W. F.; Chang, C. P.; Chu, M. W.; Chen, C. W. *J. Am. Chem. Soc.* **2009**, *131*, 3644–3649.
(8) McDonald, S. A.; Konstantatos, G.; Zhang, S.; Cyr, P. W.; Klem, E. J. D.; Levina, L.; Sargent, E. H. *Nat. Mater.* **2005**, *4*, 138–142.
(9) Oosterhout, S. D.; Wienk, M. M.; van Bavel, S. S.; Thiedmann, R.; Koster, L. J. A.; Gilot, J.; Loos, J.; Schmidt, V.; Janssen, R. A. J. *Nat. Mater.* **2009**, *8*, 818–824.
(10) Coakley, K. M.; McGehee, M. D. *Appl. Phys. Lett.* **2003**, *83*, 3380–3382.
(11) Ravirajan, P.; Peiró, A. M.; Nazeeruddin, M. K.; Graetzel, M.; Bradley, D. D. C.; Durrant, J. R.; Nelson, J. *J. Phys. Chem. B* **2006**, *110*, 7635–7639.
(12) Olson, D. C.; Piris, J.; Collins, R. T.; Shaheen, S. E.; Ginley, D. S. *Thin Solid Films* **2006**, *496*, 26–29.
(13) Hindson, J. C.; Saghi, Z.; Hernandez-Garrido, J. C.; Midgley, P. A.; Greenham, N. C. *Nano Lett.* **2011**, *11*, 904–909.
(14) Dayal, S.; Reese, M. O.; Ferguson, A. J.; Ginley, D. S.; Rumbles, G.; Kopidakis, N. *Adv. Funct. Mater.* **2010**, *20*, 2629–2635.
(15) van Bavel, S. S.; Loos, J. *Adv. Funct. Mater.* **2010**, *20*, 3217–3234.
(16) van Bavel, S. S.; Sourty, E.; de With, G.; Loos, J. *Nano Lett.* **2009**, *9*, 507–513.
(17) Moon, J. S.; Lee, J. K.; Cho, S.; Byun, J.; Heeger, A. J. *Nano Lett.* **2009**, *9*, 230–234.
(18) Loos, J.; Sourty, E.; Lu, K.; de With, G.; van Bavel, S. S. *Macromolecules* **2009**, *42*, 2581–2586.

(19) Lu, K.; Sourty, E.; Guerra, R.; Bar, G.; Loos, J. *Macromolecules* **2010**, *43*, 1444–1448.
(20) Chu, M. W.; Liou, S. C.; Chang, C. P.; Choa, F. S.; Chen, C. H. *Phys. Rev. Lett.* **2010**, *104*, 196101–4.
(21) Deibel, C.; Dyakonov, V.; Brabec, C. J. *IEEE J. Sel. Top. Quantum Electron.* **2010**, *16*, 1517–1527.
(22) Nakade, S.; Saito, Y.; Kubo, W.; Kitamura, T.; Wada, Y.; Yanagida, S. *J. Phys. Chem. B* **2003**, *107*, 8607–8611.
(23) Juška, G.; Arlauskas, K.; Viliūnas, M.; Kočka, J. *Phys. Rev. Lett.* **2000**, *84*, 4946–4949.
(24) Denler, G.; Mozer, A. J.; Juška, G.; Pivrikas, A.; Osterbacka, R.; Fuchsbaur, A.; Sariciftci, N. S. *Org. Electron.* **2006**, *7*, 229–234.
(25) Homa, B.; Andersson, M.; Inganas, O. *Org. Electron.* **2009**, *10*, 501–505.
(26) Bässler, H. *Phys. Status Solidi (b)* **1993**, *175*, 15–56.
(27) Choulis, S. A.; Kim, Y.; Nelson, J.; Bradley, D. D. C.; Giles, M.; Shkunov, M.; McCulloch, I. *Appl. Phys. Lett.* **2004**, *85*, 3890–3892.
(28) Zeng, T. W.; Lin, Y. Y.; Lo, H. H.; Chen, C. W.; Chen, C. H.; Liou, S. C.; Huang, H. Y.; Su, W. F. *Nanotechnology* **2006**, *17*, 5387–5392.
(29) Tuladhar, S. M.; Poplavskyy, D.; Choulis, S. A.; Durrant, J. R.; Bradley, D. D. C.; Nelson, J. *Adv. Funct. Mater.* **2005**, *15*, 1171–1182.
(30) Coakley, K. M.; Srinivasan, B. S.; Ziebarth, J. M.; Goh, C.; Liu, Y.; McGehee, M. D. *Adv. Funct. Mater.* **2005**, *15*, 1927–1932.